ELSEVIER

Earth and Planetary Science Letters 132 (1995) 183–198

EPSL

Experimental partitioning of Zr, Nb, and Ti between platinum group metals and silicate liquid: implications for the origin of refractory metal nuggets in carbonaceous chondrites

Stephen R. Jurewicz [a,1], John H. Jones [a,*], Bruce Fegley Jr. [b]

[a] *SN4, NASA Johnson Space Center, Houston, TX 77058, USA*

[b] *Department of Earth and Planetary Sciences and McDonnell Center for Space Sciences, Washington University, St. Louis, MO 63130-4899, USA*

Received 12 January 1995; accepted after revision 31 March 1995

Abstract

Reports of percent level concentrations of normally lithophile elements such as Zr, Nb, and Ta in some refractory noble metal nuggets in CAIs raise important questions about the redox state of the early solar nebula. Consequently, we have determined the metal/silicate liquid partition coefficients for Zr, Nb, and Ti at 1548 K and solar oxygen fugacity ($fo_2 \sim 10^{-16}$ bar). In most experiments, these elements formed intermetallic compounds with Pt-metal. Even though our partition coefficients for Zr (2.06–4.55) were substantially greater than previously determined values, they are still too small to account for percent levels of Zr in a refractory metal nugget from an average CAI. In addition, partition coefficient values obtained for Nb and Ti show an extremely strong affinity for the metal phase. Yet, Nb is rarely observed in refractory metal nuggets and Ti has never been observed. Given the abundance of Ti in CAIs, substantial concentrations of Ti should be present in refractory metal nuggets. This discrepancy is attributed to either: (1) the solar fo_2 was too oxidizing during condensation to form the predicted intermetallic compounds; or (2) the lithophile elements originally formed intermetallic compounds with Pt-metals during condensation in the solar nebula but were subsequently oxidized in a latter heating event. Whereas our experiments suggest that conditions were never reducing enough for Ti to alloy with Pt metal, other redox determinations (e.g. Ti^{3+}/Ti^{4+} ratios in CAI) imply approximately solar oxygen fugacities. Our experiments serve to emphasize the range in redox states implied by metal and silicate assemblages in CAI.

1. Introduction

Primitive meteorites and their components, such as Ca–Al rich inclusions (CAI's), from C2 and C3 chondrites, provide information on the ambient pressures, temperatures, and compositions within the solar nebula. For example, CAI's contain mineral assemblages which are enriched, relative to chondritic levels, in both refractory lithophile and siderophile elements. These enrichments indicate that CAI's represent either high temperature condensates or evaporative residues of early solar nebula materials [1,2]. The lithophile refractory elements of CAI's are contained in oxide and silicate phases, while the refrac-

* Corresponding author.

[1] Present address: U.S. Synthetic Corporation, 744 South 100 East Provo, Utah 84606

SSDI 0012-821X(95)00068-2

tory siderophile elements are concentrated in either tiny metal nuggets or in complex assemblages of metal grains and sulfides (termed fremdlinge by El Goresy et al. [3]). Although the fremdlinge appear to have a complex history [4,5], the metal nuggets appear to have a simpler origin [6–9] and, therefore, may provide a better tool for constraining the conditions that prevailed in the solar nebula at the time of their formation.

The nuggets are predominantly composed of platinum-group metals (Pt, Ir, Os, Ru, Rh, W, Mo, and Rh), with substantial Fe and Ni [6,8,10]. However, El Goresy and colleagues reported small amounts of normally lithophile elements such as Zr, Hf, Nb, and Ta in some refractory platinum metal nuggets (RPMN's) and fremdlinge in CAIs from the Allende (CV3), Ornans (CO3), and Essebi (CM2) chondrites [3,11–13]. In addition, Wark and Lovering [7] observed that some metal nuggets were closely associated with refractory oxides such as ZrO_2, $CaTiO_3$, ThO_2,and $Ca_2Nb_2O_7$.

The apparent necessity of extremely reducing conditions to incorporate refractory lithophile elements into platinum group metals was noted by Grossman [2], who emphasized that in the solar nebula, Zr should be 10^7 times more stable as ZrO_2 than as metallic Zr. Therefore, if the refractory metal nuggets formed in the solar nebula as condensates or distillates, then: (1) either the nuggets formed in a region of the solar nebula that was more reducing than for solar or (2) another thermochemical mechanism, other than simple reduction of the oxide to the metallic state, was necessary to alloy the lithophile elements with platinum group metals.

A possible explanation for this unusual siderophile behavior of normally lithophile elements was suggested by Jones and Burnett [14] who studied actinide partitioning between platinum and silicate liquid. They observed that U strongly partitioned into platinum metal at oxygen fugacities much higher than expected. They attributed this behavior to the very non-ideal alloying characteristics and formation of intermetallic phases of certain elements with platinum group metals, previously predicted by the Engel theory of metals [15,16]. For clarity, it is important to note that intermetallic phases or alloys are commonly referred to as intermetallic compounds because they are at least partially ordered. Usually, intermetallic compounds are not strictly stoichiometric but have a range of compositions [17].

Jones and Burnett hypothesized that, given the very low activity coefficient reported for Zr in platinum (approximately 10^{-12}; [16,18]) Zr may indeed alloy with platinum near solar fo_2. Later, Fegley and Kornacki [19] calculated the fo_2–T curves for several intermetallic compounds of refractory lithophiles and Pt-group metals. They found that several lithophile elements (Zr, Ti, Hf, Nb, U, and Ta) present in CAI's, could form intermetallic compounds with noble metals at solar fo_2. They also noted that although Ti-noble metal compounds are stable at nebular fo_2, metallic Ti has not been observed in any metal nuggets.

Palme and Schmitt [20] conducted experiments to determine the partitioning behavior of lithophile elements between platinum metal and silicate liquid. Their experiments were performed at higher fo_2 (e.g. $\log fo_2 = -5$ at 1800 K) than appropriate for a solar composition gas ($\log fo_2 = -14$ at 1800 K), and were extrapolated to nebular conditions by assuming specific redox reactions. Because of this extrapolation, upper and lower limits for the partition coefficients were reported. The Palme and Schmitt [20] results indicated that Nb, Ta, Cr, and V all have partition coefficient values large enough to produce the observed quantities of these elements in CAI's. However, given the small concentration of Zr in bulk CAI's (77 ppm, type B), the Zr partition coefficient (D) range was too small (0.3–2.3) to produce the reported percent level concentrations in some nuggets.

Treiman et al. [21] also conducted experiments to measure the partition coefficients for Zr and Hf between Pt–Fe metal and silicate liquid. Their experiments were run with Cr-metal as a buffer, because the Cr–Cr_2O_3 buffer is very close to solar fo_2 at the run temperature of 1600 K. Treiman et al. measured a $D_{Zr}^{Pt/Sil}$ of 0.3 which was consistent with the calculated lower limit of Palme and Schmitt. However, the Cr–Cr_2O_3 buffers of [21] were often exhausted during the experiment and it was possible that their results only represented a lower bound to the true partition coefficient.

Here we present new partitioning experiments that place stronger constraints on the possible siderophile behavior of Zr, Nb, and Ti.

2. Experimental technique

Modifications of the basic experimental technique of Treiman et al. [21] were adopted for this work. A new starting glass composition was chosen, similar to the CAI minimum melt composition of Stolper [22], having a liquidus temperature of about 1523 K (1250° C). Our composition is more silica-rich and alumina-poor than most type B CAIs which contain metal nuggets [2,7]. Also, for our experiments, FeO was substituted for the TiO_2 in Stolper's mix. Because all the Fe should be in the metallic state in our experiments, analysis for FeO in our experimental glasses provided confirmation that there was good equilibration between the buffer and the experimental charge. All starting compositions used in this work are given in Table 1. These starting compositions were prepared from pure oxide powders and were later doped with oxides of the elements to be studied. Platinum was initially used as the metal phase because it is readily available and because more thermodynamic data exist for Pt compounds than for the other members of the Pt group. The platinum metal and the oxide mix were initially blended together, with enough platinum powder added to achieve an atomic platinum-to-iron ratio of 5:1. This starting mix and the dopant oxide (i.e. ZrO_2, TiO_2, or Nb_2O_5) were stirred under acetone until uniformly mixed.

Table 1
Starting compositions

Oxide	Standard Glass[4]	Fe-free Glass[4]	$CaTiO_3$ Mixed[4]
SiO_2	41.30(0.20)[1]	42.79(0.32)	30.0
CaO	27.75(0.18)	28.79(0.14)	27.58
MgO	9.79(0.10)	9.87(0.10)	8.24
Al_2O_3	17.68(0.10)	18.55(0.10)	17.24
FeO	3.48(0.08)[2]	0.00	0.00
TiO_2	0.00	0.00	16.94
Total	100	100	100

[1] Numbers in parentheses are 2σ standard deviation.
[2] Possible minor ($< \sim 0.5$ wt%) Fe-loss.
[3] All totals converted to 100%.
[4] Mixed values represent the calculated weighed proportions while glass values represent analyses of glassed pellets of the oxide mix.

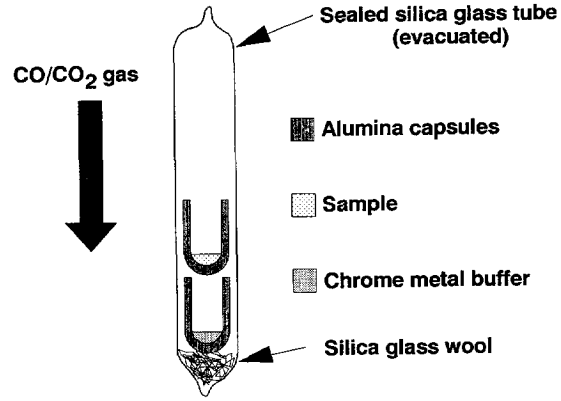

Fig. 1. The sample capsule design used for the experiments in this study.

The experimental arrangement is shown in Fig. 1. All loaded capsules were dried in a vacuum oven for 24 hours at 378 K. The sample capsule plus another capsule containing the Cr-metal buffer were placed into a silica glass tube which was then evacuated and sealed. The sealed glass tube was then hung from an alumina rod and inserted into a Deltech controlled-atmosphere furnace such that the CAI-analog-containing capsule was located in the hot spot. Temperature was measured using a gold-calibrated Pt–Pt,10%Rh thermocouple with an uncertainty of $\pm 2°$ C. A small temperature difference will exist between the sample and the buffer, but the fo_2 at all positions in the capsule should simply be the fo_2 of the $Cr–Cr_2O_3$ buffer at the temperature of that position. To prevent buffer exhaustion caused by oxygen diffusion through the silica glass tube, the sealed silica tubes were run in a flowing CO/CO_2 mixture that produced an fo_2 of IW + 2.

Experiments were run at 1548 K, ensuring that the silicate was entirely liquid. Run durations were either 48 or 96 hours. Even in the longest experiments, less than 20% of the buffer was expended. At the end of each run the samples were quenched in water. No quench crystals were observed in any of the runs.

The sample crucible and buffer were mounted in epoxy, sectioned, and polished for analysis. Analyses were performed using a Cameca electron micro-

probe, using standard techniques. However, analysis of Zr in Pt was difficult because of interference between the Zr L-alpha and Pt M-alpha lines. This problem was overcome by using the PET crystal for both elements, thus minimizing the interference, and by performing numerous Zr analyses on a pure Pt standard to obtain a correction factor for the "phantom" Pt contribution to the Zr peak. As it turned out, most of our experimental samples had several weight percent Zr in the Pt-metal. Therefore, the actual Zr content was usually 2–3 times the "phantom" Pt observed on the Pt standard, making the corrections very reliable.

Three different series of experiments were run. The first experiments (series I) used the standard iron-bearing starting composition with Ti and Nb oxides doped at 1, 5, and 10 wt%. Zirconium experiments were run at the 0.5, 1, 2.5, 5, and 8.0 wt%. Baddelyite crystallized in the 8.0 wt% experiment. In the second group of experiments (series II), a roughly equimolar blend of Os, Ru, Ir, and Pt was substituted for the Pt powder in order to determine what effect a complex alloy would have on lithophile element partitioning. The final group of experiments (series III) was similar to the first, except that an FeO-free CAI starting mix was used. The complex alloy experiments and the Fe-free experiments were doped at the 1.0 wt% level only.

A single perovskite-bearing experiment was also run. Fegley and Kornacki [18] hypothesized that the lack of Ti in any RPMN's from CAI's may be due to the presence of perovskite, which could effectively tie-up all the Ti and reduce its chemical activity. Accordingly, a CAI-like glass that would crystallize a substantial volume of perovskite at 1548 K was prepared [23].

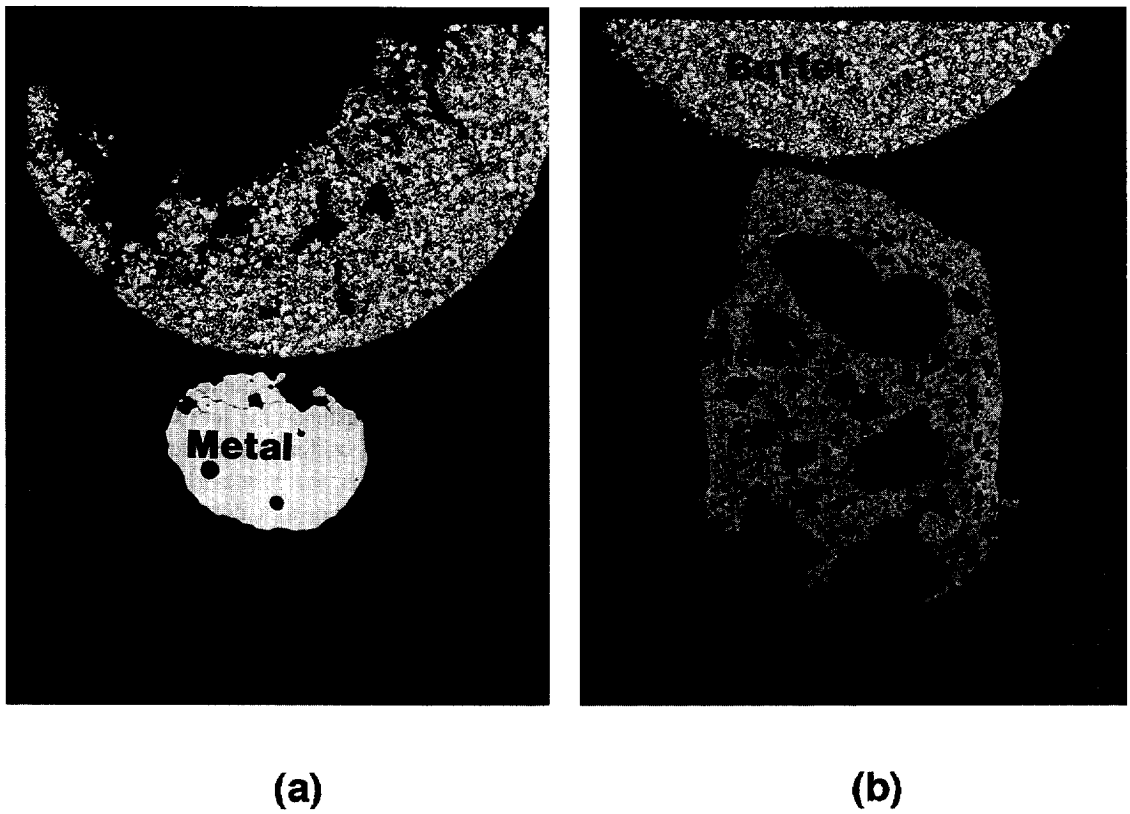

Fig. 2. (a) A reflected light photograph showing the 1.0 wt% TiO_2-doped experiment that was run for 48 hours. (b) Reflected light photograph of the 5.0 wt% TiO_2 experiment.

A final experiment was performed to evaluate the oxidation rate of Pt intermetallic compounds. A charge of Fe-bearing CAI analog, mixed with 1.0 wt% TiO_2 and Pt-metal, was run for 48 hours in an identical manner as the series I experiments. After quenching, the charge was visually inspected to determine that intermetallic compounds had formed. The sample crucible was then hung in the furnace such that the charge was at 1548 K and exposed to a flowing CO/CO_2 gas mix that was set at IW + 2, approximately 5.5 log units above the original fo_2. The charge remained in this configuration for 5 days, after which it was water quenched.

3. Results

Figs. 2a and b shows typical experimental charges from series I–III. Fig. 2a shows a 1.0 wt% TiO_2-doped experiment (Series I) after a 48 hour run. The high reflectivity of the buffer (mounted with and above the experimental charge) shows that the Cr-metal was not exhausted during the experiment. This observation was confirmed by microprobe analyses. Figs. 2a and b both demonstrate that the silicate glass reacts with the alumina crucible to form a rim of spinel between the silicate and the alumina, effectively creating a spinel crucible. The presence of anorthite laths, which grow from the bottom of the crucible, is consistent with the phase diagram [22]. The addition of alumina from the capsule and subtraction of Mg to form spinel, drives the silicate composition further into the anorthite + spinel stability field.

The Pt metal in the experiments consistently formed either of two textures. In Fig. 2a, the Pt powder formed a single metal nugget lying in the center of the capsule. This single metal nugget texture is representative of all the experiments where the concentration of the dopant oxide was below 2.5 wt%, and as discussed later, appears to be related to the presence of a Pt–Si liquid. Fig. 2b shows a 5.0 wt% TiO_2 experiment. Unlike the previous example, the platinum metal formed a column or mound rising

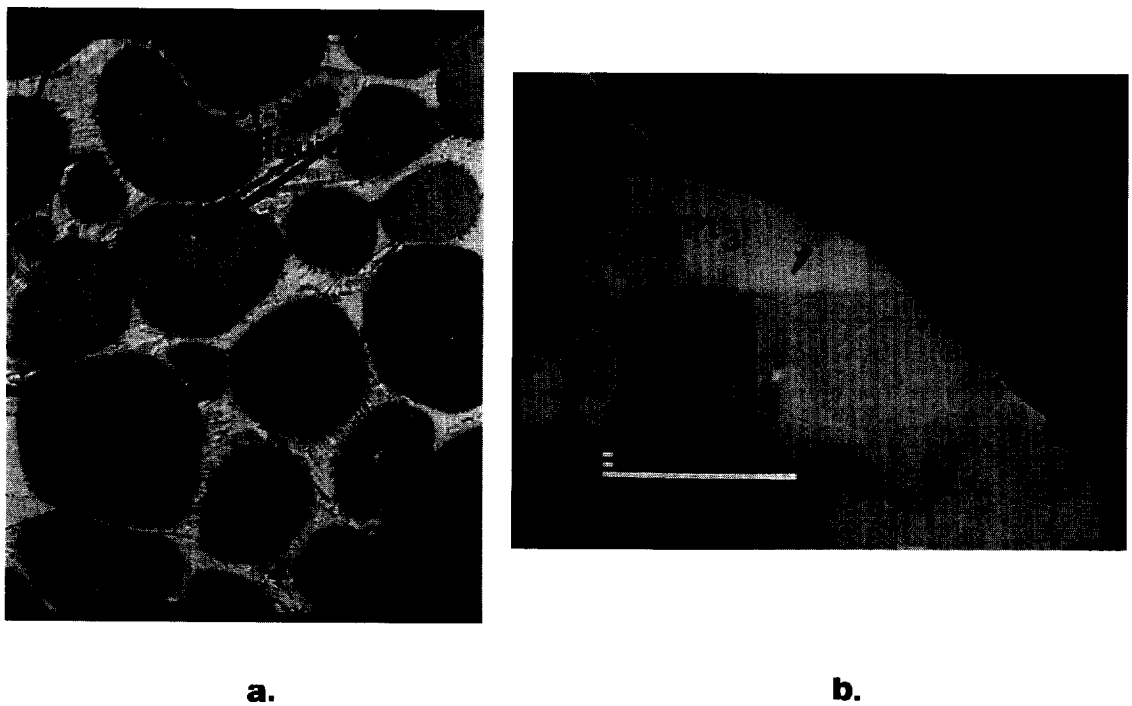

a. b.

Fig. 3. (a) BSE image of the typical metal microstructure observed in the series I experiments which contained 1.0 wt% of dopant transition metal. (b) BSE image of the microstructure from the series I, 5.0 wt% ZrO_2 experiment.

in the middle of the crucible. This column is composed of metal, glass pockets, and some voids. The other features of the experiment are the same. In both cases it appears that surface tension causes the metal to coalesce in the silicate liquid. Although the general macroscopic appearance of all the partitioning experiments in this study fall into one of these two descriptions, there were important microscopic differences among the metal phases which will be discussed next.

3.1. Series I experiments (Pt-metal with Fe-bearing CAI starting mix)

The backscattered electron (BSE) image of the 1.0 wt% TiO_2 experiment shown in Fig. 3a demonstrates that the single metal nugget shown in Fig. 2a is actually two phases: rounded grains of Pt alloy surrounded by quench products of a Pt–Si liquid. Electron probe analysis suggests that the rounded grains are a $(Fe,Ti)Pt_3$ intermetallic compound surrounded by Pt–Si–Fe quench crystals. Analysis of the rounded grains indicated that they were quite homogeneous (Table 2).

The Pt–Si compounds were observed in all experiments where the platinum metal formed a single nugget, but Ti, Zr, and Nb were below detection levels in these phases. However, in experiments with ≥ 2.5 wt% doped oxides, the Pt–Si phases were sparse or completely absent. The resulting metal texture for those experiments is similar to that shown in Fig. 3b (5.0 wt% ZrO_2 run), where the metal is a skeletal network of intermetallic grains. Variations in gray tone among the rounded intermetallic phases in the BSE images reflect crystal orientation differences as electron probe analysis did not detect any compositional differences.

Table 2 gives metal compositions from the Series I experiments. Examination of Table 2 reveals that the percentage of Pt in most of the metals is rather constant. For example, metals formed in the Zr experiments contain about 75 mole percent Pt and 25 percent (Fe + Zr), suggesting $ZrPt_3$ is the stable phase.

A similar intermetallic phase was observed in the Ti partitioning experiments. Table 2 shows that the 1.0 wt% TiO_2 experiment follows the XPt_3 pattern observed in the previous Zr experiments. According to the Pt–Ti phase diagram [24], the stable phase given the atomic percentage of Pt is $TiPt_{3-x}$, but the stability range of this compound is unknown. The minus sign in the formula indicates that the phase usually has a little less than 3 Pt atoms per molecule, which is also indicated in our results (see Table 2).

Table 2
Metal compositions from series I experiments

Doped Wt.%	Wt.% Pt	At.% Pt	Wt.% Fe	At.% Fe	Wt.% Ti	At.% Ti	At.% Ti+Fe
1.00	91.03(0.48)[1]	75.47	6.36(0.14)	18.42	1.81(0.16)	6.11	24.53
5.00	88.70(0.66)	71.34	5.42(0.26)	15.06	4.20(0.40)	13.60	28.66
10.00	88.43(1.16)	69.04	5.14(0.18)	11.85	5.33(0.16)	16.95	28.80
	Wt.% Pt	At.% Pt	Wt.% Fe	At.% Fe	Wt.% Zr	At.% Zr	At.% Fe+Zr
0.50	90.70(0.80)	75.86	7.95(0.18)	23.23	0.51(0.22))	0.91	24.14
1.00	91.55(0.72)	77.46	6.81(0.04)	20.13	1.33(0.14)	2.41	22.54
2.50	89.31(1.00)	75.71	6.19(0.08)	18.33	3.29(0.10)	5.96	24.29
5.00	88.75(0.80)	75.45	5.17(0.80)	15.36	5.05(1.00)	9.18	24.55
8.00	88.54(1.20)	74.57	4.89(0.60)	14.39	6.13(0.80)	11.04	25.43
	Wt.% Pt	At.% Pt	Wt.% Fe	At.% Fe	Wt.% Nb	At.% Nb	At.% Nb+Fe
1.00	92.46(1.20)	81.50	5.33(0.60)	16.41	1.13(0.40)	2.09	18.50
5.00	87.52(0.80)	72.03	5.78(1.20)	16.62	6.57(1.20)	11.35	27.97
10.00	81.37(0.34)	63.56	3.35(0.48)	9.14	16.63(0.34)	27.30	36.44

[1] Numbers in parenthesis are 2σ deviations.

The metal composition from the Nb experiments is more complex. The binary phase diagram for the Nb–Pt system [24] shows a $NbPt_3$ + Pt stability field that begins at 82 atomic percent Pt. Interestingly, the metal from our 1.0 wt% Nb_2O_5 experiment has 81.5 atomic percent Pt, putting it in the $NbPt_3$ + Pt stability field. However, no pure Pt was observed and it is difficult to determine if this is due to the presence of Fe in the system or to other factors. The metal of the 5.0 wt% Nb_2O_5 experiment is in the $NbPt_3$ stability field at 72.03 atomic percent Pt and $NbPt_3$ appears to be the stable phase, based on the atomic percentage of Fe + Nb. The metal of the 10.0 wt% Nb_2O_5 experiment has 63.56 atomic percent Pt, which puts it approximately in the $NbPt_2$ stability field, agreeing moderately well with the measured composition of the metal.

The noble-metal/silicate liquid "partition coefficient" results from our experiments are summarized in Table 3. Although Ti, Nb, and Zr are major elements in the metal alloys, we use the partition coefficient formalism because it provides a useful means of comparing our work to that of others.

D_{Zr} for the Series I experiments (Table 3) indicates that Zr does indeed partition into the metal phase at solar redox conditions. However, the values of the partition coefficients, while greater than 1, are still relatively small. The D_{Ti}'s of Table 3 are quite large and Ti strongly partitions into Pt-metal under these conditions. The D_{Nb}'s in Table 3 are a bit misleading. No true Nb peaks above background could be detected in the silicate. Therefore, the D's reported represent *minimum* partition coefficients, calculated assuming a fictitious Nb peak 3-σ above background on the silicate. The actual D's are probably much larger than those reported. Even so, it is readily apparent that Nb strongly partitions into Pt metal.

Table 3
Summary of partitioning results

Starting Wt.%	Partition Coefficient[4] Zr	Nb	Ti
	Series I		
0.5	2.09(0.47)[3]		
1.0	3.82(0.52)	>10[1]	151(60)
2.5	4.55(0.51)		
5.0	3.91(0.38)	>55	6(5)
8.0	2.06(0.33)		
10.0		77(30)	1.49(0.10)
	Series II		
1.0	nd[2]	>40	14(5)
	Series III		
1.0	3.25(1.24)	>22	400(145)

[1] Nb_2O_5 concentrations in the silicate were at the detection limit of the electron probe (see text).
[2] Zr in the metal phase is below the detection limit of the electron probe.
[3] Numbers in parentheses are 2σ standard deviations.
[4] Partition coefficients defined as wt% tracer in metal/wt% tracer oxide in silicate glass.

Table 4
Average metal compositions from the complex alloy experiments

X	At.% Pt	At.% Fe	At.% X	At.% Ru	At.% Os	At.% Ir
Zr	42.63	33.80	0.00	15.01	1.41	7.15
Lo-Ti[2]	35.12	18.78	5.72	12.22	7.94	20.21
Hi-Ti[2]	47.22	21.36	8.43	4.13	1.97	16.90
Nb	46.80	21.64	7.74	4.52	1.41	17.89
X	**Wt.% Pt**	**Wt.% Fe**	**Wt.% X**	**Wt.% Ru**	**Wt.% Os**	**Wt.% Ir**
Zr	60.83(3.82)[1]	13.81(0.66)	0.00	11.10(2.26)	1.96(0.90)	10.05(2.72)
Lo-Ti[2]	46.25(6.54)	7.08(1.02)	1.85(0.62)	8.34(4.84)	10.19(6.28)	26.22(6.32)
Hi-Ti[2]	61.84(5.60)	8.01(1.24)	2.71(0.84)	2.80(1.6)	2.51(3.5)	21.80(5.88)
Nb	59.68(2.94)	7.90(0.88)	4.70(1.06)	2.99(0.50)	1.75(0.80)	22.47(2.6)

[1] Numbers in parenthesis are 2σ deviations; [2] The Ti experiments appeared to bimodally form high-Pt and a low-Pt groups and are reported as such.

3.2. Series II experiments (Pt, Os, Ir, and Ru metal with Fe-bearing CAI mix)

Reflected-light analysis of the metal microstructures of the experimental charges from the complex alloy experiments shows they resemble the higher concentration series I experiments. In both cases the metal alloy formed columns in the center of the capsule. In BSE imaging the metal consists of light and dark gray areas. Electron microprobe analyses indicate that the light areas are Pt,Fe-rich and Os,Ru-poor, while the darker areas are Pt-poor and Os,Ru-rich. Iridium seems to show a weak preference for the Os, Ru-rich phase based upon relative concentrations. Zirconium was not observed in the metal phase and analysis of the glass indicated that no ZrO_2 was lost to the metal. Therefore, no D_{Zr}'s are reported for Series II in Table 3.

The Series II Ti partitioning experiments were macroscopically and microscopically similar to the Zr experiments. However, as shown in Table 4, Ti enters the Pt–Fe phase. Electron microprobe analyses indicate that an Os, Ru-rich phase is also present but contained no Ti. The Ti partition coefficients for the Series II experiments (Table 3) show substantial variation. This is due to several factors: (1) the Ti experiments developed the largest metal columns and there is substantial variation in Ti content from the top to the bottom of the column; and (2) the TiO_2 content of the glass is low (about $0.3 \pm 0.1\%$). However, it is apparent that, even with a complex alloy, Ti strongly partitions into the metal phase.

The Nb Series II experiments were similar in texture to previous experiments. As can be seen in Table 4, Nb was observed to strongly partition into the metal. Again, because no Nb was observed in the silicate, only lower limits to D's are presented.

3.3. Series III experiments (Pt-metal and Fe-free CAI mix)

The experimental charges from the Fe-free series of experiments formed a single metal nugget in the silicate glass similar to the low concentration experiments from Series I. The microstructure of this experiment is somewhat different from the previous experiments. Three distinct phases are present in BSE imaging: a dark-gray phase, a medium-gray phase, and a light-gray phase. This texture is common to both the Nb and Zr, Fe-free experiments. Chemical analyses of the medium- and light-gray phases show that they are Pt–Si quench phases. The dark phase is a $(Si,Cr,Nb)Pt_3$ intermetallic compound and its composition is given in Table 5 along with the rest of the Pt metal analyses in this series. The Cr in the metal apparently came from the buffer via vapor phase transport. The increased solubility of Cr in Pt is plausibly due to the lack of Fe in the system. A similar relationship between Fe and Cr was observed by Hanson and Delano [25]. Once again, the D values listed are lower limits because no Nb was left in the silicate.

The Series III Zr experiment closely resembled the Nb experiment. The darkest phase in the Zr experiments was a $(Si,Cr,Zr)Pt_3$ compound. While some of the dark material appeared dendritic, a few large euhedral grains were found. The D in Table 4 was calculated using the large intermetallic grains and the glass composition.

The TiO_2 experiment from this series was different because it had a metal texture similar to the low transition metal concentration Series I experiments. In this experiment, the metal is probably a $TiPt_8$ intermetallic phase or Pt–Ti alloy. As shown in Table 5, this phase is pure Pt–Ti and does not contain any Si or Cr. D_{Ti} for this series is about 400, which is the largest Ti partition coefficient measured in this work. Titanium has an extremely strong tendency to partition into Pt-metal in an Fe-free system.

Table 5
Metal compositions from the Fe-free starting mix

X	At.% Pt	At.% Si	At.% X	At.% Cr
Ti	84.07	0.00	15.93	0.00
Zr	76.79	9.11	4.71	9.40
Nb	75.97	12.88	4.54	6.61
X	Wt.% Pt	Wt.% Si	Wt.% X	Wt.% Cr
Ti	94.03(0.52)[1]	0.00	4.36(0.40)	0.00
Zr	90.43(0.74)	1.56(1.5)	2.62(0.98)	2.98(0.76)
Nb	91.35(1.16)	2.23(0.92)	2.60(0.70)	2.12(0.48)

[1] Numbers in parenthesis are 2σ deviations.

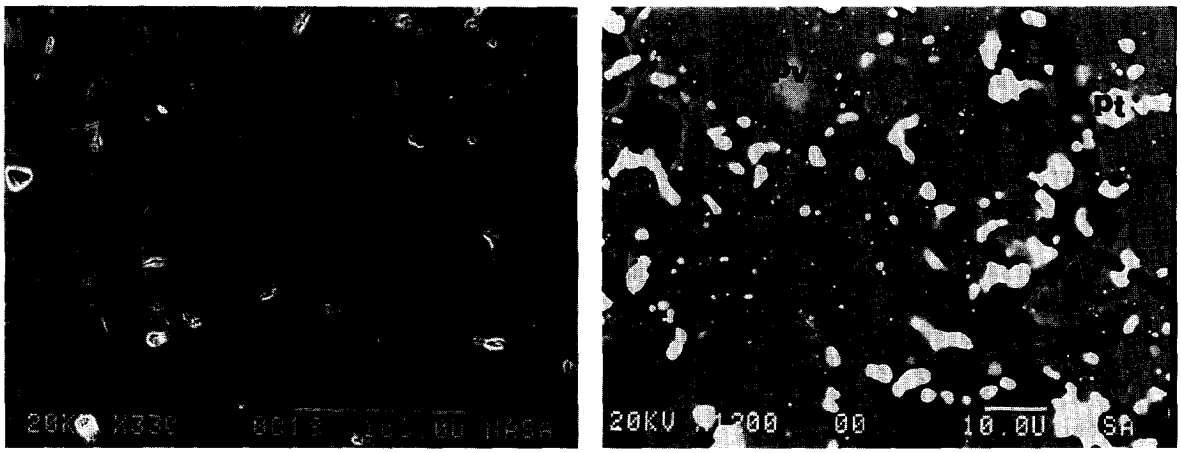

Fig. 4. (a) BSE image showing the microstructure of the melted and crystallized perovskite starting material before it was ground to a powder. (b) BSE image of the perovskite experiment after being run in a sealed silica tube for 48 hours.

3.4. Perovskite results

The goal of the perovskite experiment was to determine if Ti would partition into Pt metal when the Ti was stabilized in the mineral perovskite. Fegley and Kornacki [18] speculated that the absence of Ti in RPMN's could be due to Ti stabilization in perovskite. After crystallizing for 5 days the starting material had a texture as shown in Fig. 4a. The crystallized glass was composed of perovskite

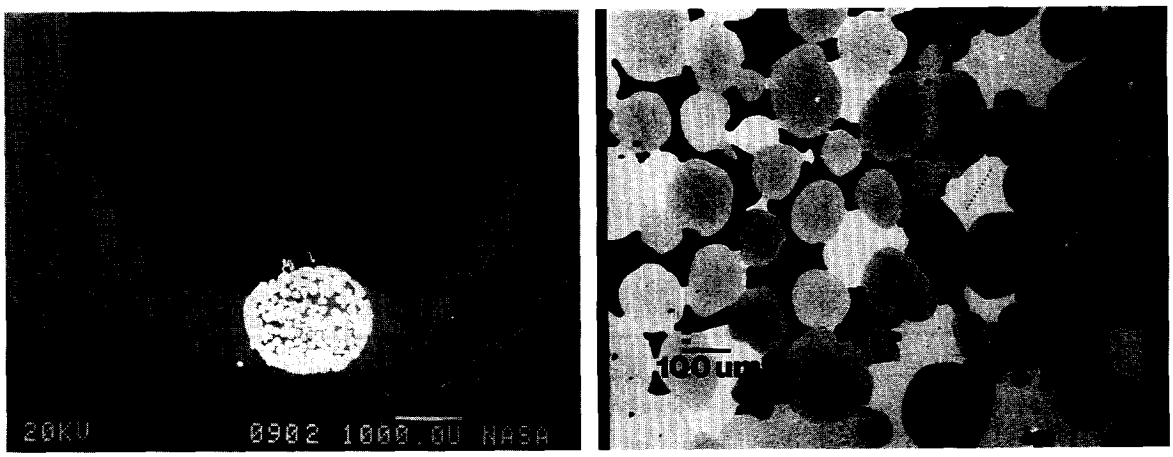

Fig. 5. (a) A secondary electron image showing the charge from the oxidation experiment. (b) A higher magnification backscattered electron image showing that the metal bleb is actually composed darker gray $(Fe,Ti)Pt_3$ grains held together by a lighter gray material which is a Pt–Fe–Ti alloy.

(brightest phase in Fig. 4a), spinel (euhedral triangular crystals in Fig. 4a), fassaite (6.22 wt% TiO_2), and olivine. Fig. 4b shows the texture after the material in Fig. 4a was heated with Pt. The brightest phase is Pt-metal and a second, less bright, phase is perovskite. The dark gray phase is anorthite and the medium gray phase is fassaitic pyroxene (11.2 wt% TiO_2), and there was also some spinel. Comparison of Fig. 4a and b shows that the amount of perovskite has substantially decreased. The metal phase is primarily platinum with Ti (18.2 at.%) and significant Cr (13.5 at.%) making up the balance.

3.5. Oxidation experiment results

Fig. 5a shows a general view of the experimental charge from the oxidation experiment. While the charge appears similar to the previous 1.0 wt% TiO_2 run, there are some distinct differences. Most notably, the metal bleb is eroded, exposing the interior grains. At higher magnification (Fig. 5b) BSE imaging shows that the structure consists of darker gray interior grains held together with a lighter gray interstitial material (the darkest regions are silicate). Electron microprobe analysis indicates that the darker grains are the $(Fe,Ti)Pt_{3-x}$ intermetallic phase and the lighter gray phase is a Pt–Fe–Ti alloy (95–5–0.6 wt%, respectively). No Pt–Si phases were found in the metal. The silicate/oxide phases consisted of anorthite and glass with a spinel rim at the glass/crucible interface. The glass composition away from the metal was similar to the glass from the previous 1.0 wt% TiO_2 experiment. However, the glass rimming the metal was higher in SiO_2 (54 wt% compared to 44 wt%) and TiO_2 (1.8 wt% compared to 0.15 wt%). The glass in the interior of the metal was also richer in SiO_2 and TiO_2. These results suggest that the eroded texture of the metal bleb and the high SiO_2 concentration of the glass in and around the metal presumably resulted from the decomposition of the original Pt–Si phase. Although most of the Pt–Ti intermetallic phase remained, the increased concentration of TiO_2 in the glass rimming the metal suggests that it was also decomposing but at a slower rate than the Pt–Si phase.

4. Discussion

The results discussed earlier show that solid solutions of Pt intermetallic compounds such as $TiPt_3$,

Table 6
Thermodynamic properties of selected Pt-metal intermetallic compounds $\Delta G^\circ = A + BT$

Compound	A (J mole^{-1})	B (J mole^{-1} K^{-1})	ΔG° uncertainty ±kJ mole^{-1}	Reference(s) & notes
TiPt	-159,300	16.8	14.4	[39] (a)
$TiPt_3$	-341,830	33.5	7.1	[18]
ZrPt	-191,900	20.6	13.9	[39] (a)
$ZrPt_3$	-433,230	41.1	5.5	[30,31,40] (b)
$NbPt_3$	-194,140	40.2	15	[16,19]
SiPt	-118,700	0.8	6.7	[41,42] (c)
$SiPt_2$	-185,200	1.2	8.5	[41,42] (c)
$SiPt_3$	-212,000	1.6	20.9	[42] (d)

(a) Based on the calorimetrically determined enthalpy of formation reported by [39] and assuming the same ΔS per gram atom as measured for either TiPt3 or $ZrPt_3$, respectively, by [18,40].

(b) The equation is a linear least squares fit to the free energy data given in references [40,30,31]. These independent data show good agreement. However, the ΔG° fit is 83.5 kJ mole^{-1} less negative than the calorimetrically determined enthalpy of formation reported by [31].

(c) Based on the calorimetrically determined enthalpy of formation reported by [41] and the average ΔS of formation of $-0.4 + 1.7$ J g atom^{-1} K^{-1} for M – Si compounds listed in [42].

(d) Based on the estimated enthalpy of formation in [42] and the average ΔS of formation of $-0.4 + 1.7$ J g atom^{-1} K^{-1} for M–Si compounds listed in [42].

$ZrPt_3$, $NbPt_3$, etc. formed in the experiments. The stability fields of the Pt intermetallic compounds were calculated from reactions exemplified by:

$$MO_x(s) + 3Pt(s) = MPt_3(s) + x/2O_2(g) \quad (1)$$

where M = Ti, Zr, Nb, or Si and x = the number of oxygen atoms per metal atom in the pure oxide. The equilibrium fo_2 for coexistence of the pure metal oxide, pure Pt, and the intermetallic compound is given by the equation:

$$\log fo_2 = (2/x)\log K_1 = -(2/x)\Delta G^0/(19.144T) \quad (2)$$

where ΔG^0 is in joules mole^{-1} and T is in Kelvin. The standard Gibbs free energy for reaction (1) was calculated from thermodynamic data for the metal oxides [26] and for the Pt intermetallic compounds (Table 6). The 2σ uncertainties in the thermodynamic data correspond to uncertainties of about ± 0.2 to ± 0.7 $\log fo_2$ units at the experimental run temperature of 1548 K.

The results of the calculations are illustrated in Fig. 6 where the equilibrium fo_2 values are plotted from 1000 to 2000 K. At higher oxygen fugacities, the stable phases are the metal oxide plus Pt metal. At lower fo_2's the intermetallic compound is the stable phase. Over this temperature range, $TiPt_3$ is the most stable intermetallic compound, i.e. it is stable to the highest oxygen fugacities. The next most stable compound is $NbPt_3$ followed by $SiPt_3$, and finally $ZrPt_3$. Within the mutual uncertainties, $SiPt_3$ and $ZrPt_3$ form at the same fo_2 over the 1000–2000 K range. Fig. 6 also shows the oxygen fugacity of the Cr–Cr_2O_3 buffer calculated using data from Robie et al [26]. At the run temperature of 1548 K, $TiPt_3$, $NbPt_3$, $SiPt_3$, and $ZrPt_3$ are all stable at the fo_2 of the buffer. The calculated fo_2 of a solar gas is also shown for comparison. The elemental abundances of Anders and Grevesse [27] were used in the calculations, which were done with the CONDOR chemical equilibrium code described by Lodders and Fegley [28]. At temperatures and pressures where the dissociation of water vapor to OH + H and of hydrogen to atomic H is negligible, the fo_2 of a solar gas can be calculated from the H_2O/H_2 ratio using the equation $\log fo_2 = 2\log(H_2O/H_2) + 5.59 - 25{,}598/T$ [29]. The solar gas and the Cr–Cr_2O_3 buffer have the same oxygen fugacity at the run temperature. Thus, in the presence of pure Pt, the intermetallic compounds $TiPt_3$, $NbPt_3$, $SiPt_3$, and $ZrPt_3$ are all predicted to be stable both in the experiments and in the solar nebula.

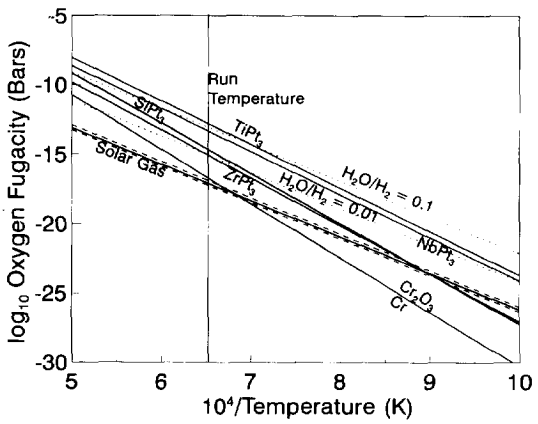

Fig. 6. A calculated $\log fo_2$ versus inverse temperature plot showing the stability fields of various intermetallic alloys of Pt in reference to solar gas and Cr–Cr_2O_3. See text for a description of the calculations.

4.1. Interpretation of the experimental results

The major discrepancy between the experimental partition coefficients and the thermodynamic predictions is the failure of Zr to strongly partition into the metal phase in our experiments. There are four possible explanations for this discrepancy. First, there could be errors in the thermodynamic data for the Zr–Pt intermetallic compounds which could actually be much less stable and hence require more reducing conditions for their formation. However this explanation is unlikely because three independent sets of experiments by three different groups give $ZrPt_3$ thermodynamic data that are in good agreement [16,30,31]. The $ZrPt_3$ enthalpy of formation determined by fluorine bomb calorimetry by Srikrishnan and Ficalora [32] is in fact 83.5 kJ mole^{-1} more negative than the enthalpy of formation derived from the equilibrium data of the other three groups, but if the calorimetric enthalpy of formation were used instead, it would make $ZrPt_3$ even more stable.

The second possible explanation is that the experiments were actually at a higher fo_2 than expected

for the $Cr–Cr_2O_3$ buffer. However, this is also unlikely because the buffer was not exhausted at the end of the experiments. The third possible explanation is that the Zr analyses in the Pt metal are unreliable due to problems in correcting the electron probe data. However, the higher amounts of Zr which would result from the formation of $ZrPt_3$ should be detectable above the phantom Zr background produced by pure Pt.

The fourth, and most likely, explanation is that Zr did not strongly partition into the metal phase because of the effects of the other alloying elements such as Fe, Cr, and Si. This explanation is difficult to test unambiguously because no data could be found for either the pure compounds $FePt_3$ and $CrPt_3$, or for Zr–Pt solid solutions with the other alloying elements. However, thermodynamic calculations in the Appendix on the stability of the Fe–Pt and Cr–Pt binary solutions suggest that this explanation is indeed plausible because both Fe and Cr oxides reduce to metals at higher fo_2's than does ZrO_2.

These results qualitatively indicate that the order of ease of reduction by Pt follows the sequence: $Fe > Cr \geq Nb > Ti > Zr$. Apparently Zr partitioning into the Fe–Pt or Cr–Pt alloys is much less favorable thermodynamically than Ti, Nb, or Si partitioning into the same types of alloys. Competition for sites in the Pt intermetallic compounds could then explain the lack of Zr in the metal phase despite other experimental data showing that $ZrPt_3$ is stable at the fo_2 of our experiments.

4.2. Constraints on the origin of refractory metal nuggets in CAIs

The original question posed in this work was: Are the experimentally derived partition coefficients sufficient to create the percent levels of lithophile elements observed in some RPMNs? Table 7 presents the predicted concentrations of lithophile elements in Pt-rich nuggets using the maximum and minimum values of our Series I D's and CAI trace element concentrations from Palme and Schmitt [19]. The partitioning experiments indicate that tens of percent of Ti, up to 0.6% of Nb, and up to 390 ppm of Zr should be present in Pt-rich nuggets that have equilibrated with typical Type B CAI melts. In stark contrast, most refractory metal nuggets in CAIs do not contain Ti, Nb, Zr, or Si. Only a few analyses and reports show percent levels or less of Zr, Nb, Hf, Ta, or Si in refractory metal nuggets in CAIs (e.g.; [3,11–13,33]. But in general, the vast majority of refractory metal nugget analyses show none of these normally lithophile elements. For example, Wark [10] analyzed a large number of refractory metal nuggets and did not find any Ti, Nb, or Zr. How can we explain this apparent discrepancy between a large body of experimental work and theoretical calculations on the one hand and the observations of refractory metal nuggets in CAIs on the other?

Three plausible explanations seem to be possible. In the first scenario (and the one we tend to favor), the refractory metal nuggets in CAIs originally formed in an environment more oxidizing than a solar gas. In this case, the nuggets would be devoid of any Ti, Nb, Zr, or Si because the alloys of these elements with Pt or other Pt-group metals were thermodynamically unstable. This model is supported by the common occurrence of Mo and W depletion's in CAIs. As originally demonstrated by Fegley and Palme [9] the Mo and W depletions in CAIs are due to high-temperature condensation under oxidizing conditions. The condensation origin of these depletions was subsequently verified by the experimental work by Wulf [34] who showed that the same type of depletions cannot be produced by evaporation under oxidizing conditions. The Mo and W depletions in CAIs are fairly common, but are generally not measured because most analytical

Table 7
Expected concentrations of lithophile elements in Pt-rich nuggets *

Element	Conc. Avg. type B (ppm)	Part. Coeff. (min/max)	Expected RPMN Conc. (ppm)
Zr	77	2/5	154/385
Nb	6	10/1000**	60/6000
Ti	150,000#	1.5/150	22%/225%

* Based upon experimental D values from this work.
** Arbitrary upper limit.
\# From Grossman [12]. Corresponds to the low end of the Ti concentration range in type B CAIs.

groups do not analyze for Mo and W in CAIs. However, the Mainz group is able to do this and, as noted by [29], their analytical data show that approximately 77% of all CAIs analyzed for Mo and W display Mo depletions and 15% display both Mo and W depletions. These observations are consistent with the thermodynamic calculations which show that, with increasing oxygen fugacity, the Mo depletions are produced first and the W depletions produced second [9].

Further evidence for oxidizing conditions at high temperatures in the solar nebula is provided by the FeO-rich rims on isolated olivine grains and on chondrules in the Allende CV3 chondrite. Palme and Fegley [35] showed that high-temperature condensation under oxidizing conditions is the most plausible explanation for these rims. Furthermore, the fo_2's required are in the same range as those required to produce the Mo and W depletions in the CAIs of Allende and other carbonaceous chondrites.

Finally, the work of Kornacki and Wood [36] on the composition of fine-grained CAIs in Allende also supports the concept of high-temperature oxidation in the solar nebula. These authors argue that the FeO-bearing spinels in fine-grained CAIs probably were formed by high temperature condensation in the solar nebula because of the observed chemistry and mineralogy of the inclusions. Using the published literature data, Kornacki and Wood [36] showed that the Co/Fe, Ni/Fe, and Au/Fe ratios in Allende fine-grained inclusions were generally subchondritic. In other words, Co, Ni, and Au were less abundant than expected if they had entered the inclusions in a primary Fe metal phase. Instead the analytical data suggest that Fe originally entered the inclusions predominantly as FeO-bearing phases such as hercynitic spinel. The mineral assemblages in the fine-grained inclusions are also inconsistent with low temperature oxidation of a primary Fe metal phase because this process would leave behind relict Fe–Ni metal and relict metal + spinel assemblages. However, these assemblages are either absent or very rare in fine-grained Allende CAIs. These two independent arguments led Kornacki and Wood to conclude that the hercynitic spinels were formed by high-temperature condensation under oxidizing conditions in the solar nebula.

Thus, several lines of evidence strongly suggest that most CAIs, or at least the metal phases in most CAIs, originally formed under oxidizing conditions in the solar nebula. If this model is correct, then, Ti, Nb, Zr, and Si are expected to be absent from the refractory metal nuggets in the CAIs.

In a second scenario, the refractory metal nuggets in CAIs were originally formed in a solar gas and were later exposed to more oxidizing conditions. In this case the nuggets originally contained Ti, Nb, Zr, Si and possibly other lithophile elements as well, but later lost them during a secondary oxidation event. The observations supporting this model are the Ti^{3+}/Ti^{4+} ratios in different minerals in CAIs. Beckett et al [37] used electron spin resonance to measure the Ti^{3+}/Ti^{4+} ratio in hibonite in inclusion SH-7 from the Murchison CM2 chondrite and found that the observed ratio was consistent with equilibration in a solar gas. Beckett et al [37] also summarize prior experimental and observational work on Ti^{3+}/Ti^{4+} ratios in synthetic and meteoritic hibonite, fassaite, and rhönite. All of this work implies that CAIs equilibrated with a gas at least as reducing as solar. These observations suggest that at least some of the refractory metal nuggets in CAIs formed in a solar gas, and thus originally contained Ti, Nb, Zr, and Si. The nuggets, and presumably the entire CAIs, must have later been exposed to more oxidizing conditions, perhaps in a planetary setting, in order to remove the lithophiles from the refractory metal nuggets. This scenario is analogous to the model proposed by Blum and colleagues for the origin of fremdlinge in CAIs (e.g., [5,38]).

Finally, as a third scenario, there is the possibility, as discussed above, that lithophiles did not enter the refractory Pt nuggets because the activity of Pt was sufficiently low (because of other alloying elements) that the power of Pt to aid in the reduction process was minimal. The TiO_2-doped complex alloy experiment suggests that, for this mechanism to be effective, Pt must be at very low concentrations. This experiment, whose D_{Ti} is well within the range of the simpler Series I experiments, contained only 35–50 atomic% Pt, within the range of Pt concentrations found in Allende CAIs [10]. Thus, we consider this last possibility to be least viable.

Regardless of our predilections, it is difficult to choose between these scenarios. An important consideration is the results of the secondary oxidation

experiment which suggests that any noble metal intermetallic compounds that form will tend to resist subsequent oxidation episodes. Although the kinetics of secondary oxidation reactions under parent body conditions need to be studied further to assess the long term survivability of these noble metal intermetallic compounds, the first scenario, in which the noble metal nuggets condensed under oxidizing conditions, appears more probable. An important test of this hypothesis would be to see if significant amounts of Ti, Nb, and Si will partition into Pt metal under T–fo_2 conditions that are predicted to lead to Mo and W depletions in CAIs.

Whichever scenario is correct, our results serve to emphasize the disparity of views on the prevalent oxygen fugacity during nebular condensation. Restricting our discussion to coarse-grained CAIs, it seems the these divergent viewpoints often depend on whether the main inferences are based on metal or silicate assemblages. It seems to us that the strongest evidence for low (i.e., solar) fo_2's comes from the Ti^{3+} concentrations measured in CAI fassaites by Beckett [23]. Conversely, some of the most compelling evidence for oxygen fugacities more oxidizing than solar stems from compositions of metallic phases. Perhaps there are sufficient differences in the timing/location of metal and silicate condensation that these observations can eventually be reconciled [9]. However, even this hopeful scenario probably requires that the metal nuggets be armored, sequestered, and consequently prevented from participating in later, low fo_2 processes. Future opportunities to resolve these questions include the measurement of the activity coefficients of Ti, Nb, and Zr in alloys similar in composition to those of refractory metal nuggets and more detailed studies of the oxidation rate of intermetallic alloys such as $TiPt_3$.

Appendix 1

Thermodynamic data for $ZrPt_3$ show that it is stable under our experimental conditions. However, Zr did not strongly partition into Pt-bearing phases in our experimental runs. The calculations below indicate that Fe–Pt and Cr–Pt solid solutions are stable to higher fo_2's than $ZrPt_3$(s). Thus, in our runs, Zr was partitioning into Fe–Pt and Cr–Pt alloys instead of pure Pt metal. This led to lower Zr concentrations in the metal phase and plausibly explains why no Zr is found in refractory metal nuggets in CAIs. We are unaware of relevant thermodynamic data for $SiPt_3$ or Si–Pt alloys that can be used for analogous calculations with Si.

Activity coefficient data are available at 1123 K for Fe–Pt solid solutions [43]. The stability of Fe–Pt solutions was calculated using the reaction:

$$\mathrm{FeO(melt) + Pt(metal)} = \mathrm{Fe-Pt(alloy) + 1/2O_2(g)} \quad \text{(A1)}$$

which has the equilibrium fo_2:

$$\log fo_2 = 2\left[\log K_{eq} + \log a_{FeO} - \log a_{Fe-Pt}\right] \quad \text{(A2)}$$

A pure FeO(liquid) reference state for the FeO activity in the melt and JANAF [44] data for the standard Gibbs free energy of pure FeO(liquid) yields $\log K_{eq} = 2.57 - 12{,}913/T$ from 1000 to 2000 K. Experimentally measured FeO activities in different silicate melts [summarized in [45]] and calculated FeO activities in chondritic composition silicate melts and in CAI composition melts [46] suggest that the FeO activity coefficients in our experimental melts are close to unity. If we assume that the FeO activity coefficients are indeed unity and also assume that the Fe activity coefficients in Pt do not vary significantly between 1123 K and our experimental temperature of 1548 K then we can use the available data to calculate the equilibrium fo_2 necessary to produce Fe–Pt solutions containing the amount of Fe (about 20 atom%) observed in some of the experimental charges. This fo_2 is $\sim 10^{-9.6}$ atm, which is well above the fo_2 ($\sim 10^{-16.4}$ atm) of the experimental charges.

The stability of Cr–Pt solutions was calculated using the reaction:

$$\mathrm{CrO_{1.5}(s) + Pt(metal)} = \mathrm{Cr-Pt(alloy) + 3/4O_2(g)} \quad \text{(A3)}$$

JANAF data were used for the Cr species and activity coefficient data for the Cr–Pt alloy at 1498 K to 1823 K were taken from [47,48]. These data show that at constant composition, the Cr activity coefficient in Cr–Pt alloys varies by only about a factor of 3 over 325 K. This constancy suggests that the assumption made above of a temperature-independent activity coefficient for Fe in Fe–Pt is probably reasonable. The equilibrium fo_2 necessary to produce Cr–Pt solutions containing 10 atom% Cr is $\sim 10^{-9.9}$ atm, which agrees within a factor of two with the equilibrium fo_2 calculated above for producing a $Fe_{20}Pt_{80}$ alloy.

These results qualitatively indicate that the Fe–Pt and Cr–Pt alloys produced in the experiments are more stable than the Ti–Pt, Nb–Pt, and Zr–Pt alloys. Thus, in our experiments the Zr was probably partitioning into Fe–Pt alloys instead of pure Pt. Apparently Zr partitioning into the Fe–Pt or Cr–Pt alloys is much less favorable thermodynamically than Ti, Nb, or Si partitioning into the same types of alloys. This effect could then explain the lack of Zr in the metal phase despite other experimental data showing that $ZrPt_3$ is stable at the fo_2 of our experiments.

[*UC*]

References

[1] H. Wänke, H. Baddenhausen, H. Palme and B. Spettel, On the chemistry of the Allende inclusions and their origin as

high temperature condensates, Earth Planet. Sci. Lett. 23, 1–7, 1974.
[2] L. Grossman, Refractory inclusions in the Allende meteorite, Ann. Rev. Earth Planet. Sci. 8, 559–608, 1980.
[3] A. El Goresy, K. Nagel and P. Ramdohr, Fremdlinge and their noble relatives, in: Proc. Lunar Planet. Sci. Conf. 9th., pp. 1279–1303, 1978.
[4] A. Bischoff and H. Palme, Composition and mineralogy of refractory-metal-rich assemblages from a Ca, Al-rich inclusion in the Allende meteorite, Geochim. Cosmochim. Acta 51, 2733–2748, 1987.
[5] J.D. Blum, G.J. Wasserburg, I.D. Hutcheon, J.R. Beckett and E.M. Stolper, 'Domestic' origin of opaque assemblages in refractory inclusions in meteorites, Nature 331, 405–409, 1988.
[6] H. Palme and F. Wlotzka, A metal particle from a Ca, Al-rich inclusion from the meteorite Allende and the condensation of refractory siderophile elements, Earth and Planet. Sci. Lett. 33, 45–60, 1976.
[7] D. Wark and J.F. Lovering, Refractory/platinum metals and other opaque phases in Allende Ca–Al-rich inclusions (abstract), in: Lunar and Planetary Science IX, pp. 1214–1216, Lunar Planetary Inst., Houston, 1978.
[8] M. Blander, L.H. Fuchs, C. Horowitz and R. Land, Primordial refractory metal particles in the Allende Meteorite, Geochim. Cosmochim. Acta 44, 217–223, 1980.
[9] B. Fegley Jr. and H. Palme, Evidence for oxidizing conditions in the solar nebula from Mo and W depletions in refractory inclusions in carbonaceous chondrites, Earth Planet. Sci. Lett. 72, 311–326, 1985.
[10] D. Wark, The Allende meteorite: information from Ca–Al-rich inclusion on the formation and early evolution of the solar system, Ph. D. Thesis, U. of Melbourne, 1983.
[11] A. El Goresy, K. Nagel and P. Ramdohr, Spinel framboids and fremdlinge in Allende inclusions: Possible sequential markers in the early history of the solar system, in: Proc. Lunar Planet. Sci. Conf. 10th, pp. 833–850, 1979.
[12] A. El Goresy, H. Palme, H. Yabuki, K. Nagel, I. Herrwerth and P. Ramdohr, A calcium–aluminum-rich inclusion from the Essebi (CM2) chondrite: Evidence for captured spinel–hibonite spherules and for an ultra-refractory rimming sequence, Geochim. Cosmochim. Acta 48, 2283–2298, 1984.
[13] H. Palme, F. Wlotzka, K. Nagel and A. El Goresy, An ultra-refractory inclusion from the Ornans carbonaceous chondrite, Earth Planet. Sci. Lett. 61, 1–12, 1982.
[14] J.H. Jones and D.S. Burnett, Laboratory studies of actinide metal–silicate fractionation, in: Proc. Lunar Planet. Sci. Conf. 11th., pp. 995–1001, 1980.
[15] N. Engel, Some new viewpoints on the metallic bond, Powder Met. Bull. 7, 8–18, 1954.
[16] L. Brewer and P.R. Wengert, Transition metal alloys of extraordinary stability; an example of generalized Lewis-acid–base interactions in metallic systems. Metall. Trans. 4, 83–104, 1973.
[17] L.H. Van Vlack, Elements of Materials Science and Engineering, 496 pp., Addison-Wesley, Reading, MA, 1975.
[18] P.J. Meschter and W.L. Worrell, An investigation of high-temperature thermodynamic properties in the Pt–Ti system, Metall. Trans. 7A, 299–305, 1976
[19] B. Fegley Jr. and A.S. Kornacki, The geochemical behavior of refractory noble metals and lithophile trace elements in refractory inclusions in carbonaceous chondrites, Earth Planet. Sci. Lett. 68, 181–197, 1984.
[20] H. Palme and W. Schmitt, On the origin of lithophile refractory elements in Pt-metal nuggets from Ca-,Al-rich inclusions in carbonaceous chondrites (abstract). In: Lunar and Planetary Science XV, pp. 623–624. Lunar and Planetary Institute, Houston, 1984.
[21] A.H. Treiman, J.H. Jones and B. Fegley Jr., Experimental and theoretical constraints on the origin of lithophile element-Pt alloys (abstract), in: Lunar and Planetary Science XXII, pp. 1413–1414, Lunar and Planetary Institute, Houston, 1991.
[22] E. Stolper, Crystallization sequences of Ca–Al-rich inclusions from Allende: An experimental study,Geochim. Cosmochim. Acta 46, 2159–2180, 1982.
[23] J.R. Beckett, The Origin of Calcium-, Aluminum-Rich Inclusions from Carbonaceous Chondrites: An Experimental Study, Ph.D. Thesis, Univ. Chicago, 1986.
[24] W.G. Moffatt, The Handbook of Binary Phase Diagrams, Genium, Schenectady, 1986.
[25] Hanson B.Z. and Delano J.W. (1992) Experimental data bearing on the oxidation state of chromium and vanadium in mafic volcanics (abstract), In: Lunar and Planetary Science XXIII, pp. 623–624, Lunar and Planetary Institute, Houston, 1992.
[26] R.A. Robie, B.S. Hemingway and J.R. Fisher, Thermodynamic properties of minerals and related substances at 298.15 K and 1 bar (105 Pascals) pressure and at higher temperatures, U.S. Geol. Surv. Bull. 689, GPO, Washington, D.C., 1979.
[27] E. Anders and N. Grevesse, Abundances of the elements: Meteoritic and solar, Geochim. Cosmochim. Acta 53, 197–214, 1986.
[28] K. Lodders and B. Fegley Jr., Lanthanide and actinide chemistry at high C/O ratios in the solar nebula, Earth Planet. Sci. Lett. 117, 125–145, 1993.
[29] A.E. Rubin, B. Fegley and J.R. Brett., Oxidation state in chondrites, in: Meteorites and the Early Solar System, J.F. Kerridge and M.S. Matthews, eds., Univ. Arizona Press, Tucson, pp. 488–511, 1988.
[30] H.J. Schaller, Aktivitatskoeffizienten von zirkon in palladium und platin, Ber. Bunsenges. Phys. Chem. 80, 999–1002, 1976.
[31] R.S. Carbonara and G.D. Blue, Thermodynamics of $ZrPt_3$, High Temp. Sci. 3, 225–230, 1971.
[32] V. Srikrishnan. and P.J. Ficalora, Measurement of the enthalpies of formation of $ZrPt_3$ and $HfPt_3$ by fluorine bomb calorimetry, Metall. Trans. 5, 1471–1475, 1974.
[33] J.T. Armstrong, A. El Goresy and G.J. Wasserburg, Willy: A prize noble Ur-Fremdling—Its history and implications for the formation of Fremdlinge and CAI, Geochim. Cosmochim. Acta 49, 1001–1022, 1985.
[34] A.V. Wulf, Experimentelle Untersuchungen zum

Flachtigkeitsverhalten von Spurenelementen in primitiven Meteoriten, Ph.D. Thesis, Universitat Mainz, Mainz, Germany, 1990.

[35] H. Palme and B. Fegley Jr., High-temperature condensation of iron-rich olivine in the solar nebula, Earth Planet. Sci. Lett. 101, 180–195, 1990.

[36] A.S. Kornacki and J.A. Wood, Mineral chemistry and origin of spinel-rich inclusions in the Allende CV3 chondrite, Geochim. Cosmochim. Acta 49, 1219–1237, 1985.

[37] J.R. Beckett, D. Live, F.D. Tsay, L. Grossman and E. Stolper, Ti^{3+} in meteoritic and synthetic hibonite, Geochim. Cosmochim. Acta52, 1479–1495, 1988.

[38] J.D. Blum, G.J. Wasserburg, I.D. Hutcheon, J.R. Beckett and E.M. Stolper, E.M. Origin of opaque assemblages in C3V meteorites: Implications for nebular and planetary processes, Geochim. Cosmochim. Acta 53, 543–556, 1989.

[39] L.Topor and O.J. Kleppa, Standard enthalpies of formation of PtTi, PtZr, and PtHf, Metall. Trans. 19A, 1827–1831, 1988.

[40] P.J. Meschter and W.L. Worrell, An investigation of high temperature thermodynamic properties in the Pt–Zr and Pt–Hf systems, Metall. Trans. 8A, 503–509, 1977.

[41] L. Topor and O.J. Kleppa, Thermochemistry of the systems Pd–Si and Pt–Si at 1400 K, Z. Metallkde. 77, 65–71, 1986.

[42] T.G. Chart, Thermochemical data for transition metal–silicon systems, High Temp. High Press. 5, 241–252, 1973.

[43] O. Kubaschewski and C.B. Alcock, Metallurgical Thermochemistry, 5th ed., Pergamon, New York, 1979.

[44] M.W. Chase, C.A.. Davies, J.R. Downey, Jr., D.J. Frurip, R.A. McDonald and A.N Syverud, JANAF Thermochemical Tables, 3rd ed., J. Phys. Chem. Fef. Data 14, Suppl. 1, 1985.

[45] E.T. Turkdogan, Physicochemical Properties of Molten Slags and Glasses, Met. Soc., London, pp. 89–179, 1983.

[46] B. Fegley, Jr. and A.G.W. Cameron, A vaporization model for iron/silicate fractionation in the Mercury protoplanet, Earth Planet. Sci. Lett. 72, 311–326, 1985.

[47] D.A.R. Kay and A.K. Mohanty, The thermodynamic properties of some Pt–Cr alloys in the temperature range 1450° to 1550° C, Metall. Trans. 1, 303–304, 1970.

[48] K. Schwerdtfeger and A. Muan, Activity measurements in Pt–Cr and Pd–Cr solid alloys at 1225° C, Trans. AIME 233, 1904–1906, 1965.